
Article:
Wu, Z-F., Xu, H-P., Li, J-W. et al. (1 more author) (2015) Research of 3-D Deceptive Interfering Method for Single-Pass Spaceborne InSAR. IEEE Transactions on Aerospace and Electronic Systems, 51 (4). pp. 2834-2846. ISSN 0018-9251

https://doi.org/10.1109/TAES.2015.140325

Research of 3-D Deceptive Interfering Method for Single-pass Spaceborne InSAR

Zhe-feng Wu, Hua-ping Xu, Jing-wen Li, Wei Liu

***Abstract*—The traditional Synthetic Aperture Radar (SAR) deceptive jamming can create false targets or deceptive scenes in the SAR image effectively. However, such deceptive capability could be significantly reduced or denied by single-pass SAR interferometry (InSAR). To achieve effective deception on InSAR, the impact of SAR deceptive jamming on single-pass spaceborne InSAR is analyzed. Then, a novel fast 3-D deceptive jamming algorithm based on multiple jammers is proposed. In this method, the specific geographic locations of two jammers are first determined by the limiting conditions. Next, the expected terms for the two jammers are generated based on the deceptive phase and the relative positions of antennas and jammers. Finally, the deceptive templates are decomposed into two parts, one of which is pre-produced while the other is generated by real-time modulation. After convolving those deceptive templates with the intercepted signals, the transmitting signals of the two jammers are created. The proposed method will generate false scenes in two single looking complex (SLC) images, resulting in false phase of the interferogram and producing deceptive digital elevation model (DEM). The effectiveness of the proposed method is validated by computer simulations.**

***Index Terms*—deceptive jamming, digital elevation model, single looking, interferometric phase, synthetic aperture radar interferometry.**

INTRODUCTION

SYNTHETIC Aperture Radar Interferometry (InSAR), as a further development of the traditional SAR technology, employs two or more SAR antennas to retrieve the terrain digital elevation model of the ground surface [1]-[3]. It has been widely applied to areas such as monitoring and geological investigation. Meanwhile, in order to protect important facilities from detection and observation, the development of effective jamming methods for InSAR has become more and more important [4]-[9]. Furthermore, research on jamming methods can help identify the weakness of current InSAR systems, so that more effective and robust systems with further improved performance can be developed in the future to work in the complicated ever-changing real-world scenarios.

The authors，Wu Zhefeng, Xu Huaping, and Li Jingwen, are with the School of Electronic and Information Engineering, Beihang University (Beijing University of Aeronautics and Astronautics, BUAA), Beijing 100084, China (e-mail: wuzheming001@126.com; xuhuaping@buaa.edu.cn; lijingwen@buaa.edu.cn).

The author, Liu Wei, is with the Electronic and Electrical Engineering Department, University of Sheffield, S1 3JD, U.K (e-mail: w.liu@sheffield.ac.uk).

Recently, interfering techniques for InSAR have received intensive attentions in the InSAR community. For illustration purposes, the protected target or protected scene is defined as the jammed area at the ground surface, while the deceptive scene is defined as the false point target array in the SAR image. The InSAR interfering techniques can generally be divided into barrage jamming and deceptive jamming [7], [8].

The barrage jamming technique buries the imaging part of the protected targets, decreases the correlation of InSAR signals and produces interferometric phase errors. The resultant phase noise causes significant errors to the interferometric phase of real scene and even results in failure of phase unwrapping [9], [10]. Therefore, the accuracy of DEM is significantly reduced after elevation inversion. Barrage jamming is easy to implement, but it is difficult to meet the requirement of high power output and the produced phase errors can be easily removed by a phase filter. Thus, barrage jamming may not be applicable in practice [11]-[15].

On the other hand, the conventional SAR deceptive jamming technique, detecting the parameters of a SAR system and simulating the deceptive jamming signals as echo signals, or retransmitting the intercepted signals, has become more popular [16]-[22]. Nevertheless, it may not work for InSAR deception. Some researchers have analyzed the impact of the SAR deceptive jamming on echo phases in two antennas [9]. However, the analysis of interfering effects on co-registration is not provided. The rebound jamming can destroy the original interferometric phase of InSAR, meanwhile producing new interferometric fringes. Such a jamming method produces false phase information, but it is not utilized to generate desired false DEM [23]. In [24], the principle of 3-D deception was introduced, but the implementation method is not presented and constraint conditions are not studied.

In order to achieve InSAR deceptive interference based on 3-D models, we first analyze the interfering effects of the classic SAR deceptive jamming on single-pass spaceborne InSAR. Although SAR deceptive jamming can generate deceptive scenes in two SLC images, the difference of jammer position from protected targets will cause deviation of deceptive scenes from the jammed area in SAR image, which will further affect the co-registration of the deceptive parts. Even if co-registration is fully achieved, it is impossible to produce deceptive DEM based on 3-D models Since the two InSAR antennas receive false signals from the single jammer simultaneously, the phase parts of the resultant deceptive scenes in two SLC images are cancelled through

interferometry. Therefore, the deceptive scene will be discovered in the interferogram and DEM.

To address the aforementioned problem, we propose a fast 3-D deceptive jamming algorithm based on multiple jammers in this paper, which makes full use of the unique properties of joint interference and scene observation of spaceborne InSAR. In our method, two jammers are located according to the position of protected targets to ensure the co-registration of deceptive scenes. Then, based on the desired deceptive phases and the jammer positions, the complex constant terms used to multiply the transmitting jamming signal are calculated. Finally, the transmitting jamming signal is decomposed into two parts in the azimuth time and range frequency domain. The slow-time-dependent part is derived from real-time modulation, while the slow-time-independent part is produced in advance. After convolving these deceptive templates with intercepted signals, the transmitting signals of two jammers are generated simultaneously. Compared with the classic SAR deceptive jamming technique, the joint interfering algorithm produces not only deceptive scenes in SAR images but also false interferometric phase and DEM.

Specifically, this paper is organized as follows. Geometric configuration between InSAR, jammers and protected targets are illustrated in Section II. In Section III, the jamming effects of the classic SAR deceptive jamming technique on InSAR are analyzed. Details of the proposed algorithm are presented in Section IV. Performance analysis and simulation results of the proposed method are provided in Section V and conclusions are drawn in Section VI.

Principle and Geometrical Model of 3-D Deceptive Jamming

A schematic illustration of the InSAR deceptive jamming scenario considered in our work is shown in Fig. 1. The jammer J_1 is located at the origin of the Cartesian coordinate system, while the second jammer J_2 is located at (X', Y', Z'). Points A_1 and A_2 represent the master antenna and the slave antenna of the side-looking SAR system, respectively. (x, y, z) is the location of an arbitrary protected target P. Since the SAR platform flies along the y-axis in a fixed altitude at a speed of v_a, we assume that the instantaneous locations of the master antenna and the slave antenna are $(X_s, v_a t_a, Z_s)$ and $\left(X_s + B\cos(\alpha), v_a t_a, Z_s + B\sin(\alpha)\right)$ at slow time t_a. The distances from the master antenna and the slave antenna to the jammer J_1 are respectively denoted by $R_{mj}(t_a)$ and $R_{sj}(t_a)$. $R_m(t_a)$ and $R_s(t_a)$ are the instantaneous slant ranges between the two antennas and the protected target. α denotes the inclination of the baseline. B is the length of the baseline. XOY (ground plane) is the target focus plane.

As an InSAR antenna transmits signals, the two jammers receive the echo signals respectively. The received signals are processed by changing amplitude, time delay, Doppler frequency and multiplying with different complex terms. Then, both of the jammers send back the processed signals to InSAR simultaneously. The deceptive jamming from the two jammers is combined to generate desired deceptive phases in the interferogram and obtain the false elevation in the DEM.

Since the jammer is considered as a stationary point target within one synthetic aperture time as the InSAR passes by, $R_{mj}(t_a)$ and $R_{sj}(t_a)$ are calculated by

$$R_{mj}(t_a) = \sqrt{X_s^2 + (v_a t_a)^2 + Z_s^2} \tag{1}$$

$$R_{sj}(t_a) = \sqrt{\left(X_s + B\cos(\alpha)\right)^2 + (v_a t_a)^2 + \left(Z_s + B\sin(\alpha)\right)^2} \tag{2}$$

Similarly, $R_m(t_a)$ and $R_s(t_a)$, as the instantaneous slant ranges between the two antennas and the protected target, are given by

$$R_m(t_a) = \sqrt{\left(X_s - x\right)^2 + (v_a t_a - y)^2 + \left(Z_s - z\right)^2} \tag{3}$$

$$R_s(t_a) = \sqrt{\left(X_s + B\cos(\alpha) - x\right)^2 + (v_a t_a - y)^2 + \left(Z_s + B\sin(\alpha) - z\right)^2} \tag{4}$$

Effect of SAR Deceptive Jamming on Single-Pass Spaceborne InSAR

The challenge of 3-D deceptive jamming is how to generate deceptive scenes in two SLC images and how to produce deceptive phase in the interferogram and false elevation in the DEM. To tackle these problems, the impact of traditional SAR deceptive jamming on InSAR is first analyzed, which can be utilized to improve the performance of the new jamming method. For simplicity, we only consider the jammer J_1. Generally, the deceptive scene comprises a lot of false point targets. Without loss of generality, we only consider a single point target below.

Position Bias in Range

When spaceborne InSAR works in the single-pass mode where one antenna serves as a transmitter and both antennas record the scattered signals simultaneously, the position of the jammer will affect the location of the false point target along range. Suppose that the master antenna transmits the SAR signal $s_0(t_r, t_a)$ and the jammer J_1 retransmits the intercepted signals. Then according to Fig. 1, the transmitted signal received by jammer J_1 can be expressed as

$$J_r(t_r, t_a) = s_0(t_r, t_a) \otimes \delta\left(t_r - \frac{R_{mj}(t_a)}{c}\right) \tag{5}$$

where t_r is the fast (range) time, $\otimes$ denotes the convolution operation, $\delta(t)$ is the unit impulse function, and c is the speed of light. To jam the protected target at (x, y, z), the jammer retransmits the intercepted signal with time delay $\Delta\tau(t_a)$. Then, the false echo signal received by the master antenna can be expressed as

$$\begin{aligned} J_M(t_r,t_a) &= GJ_r(t_r,t_a)\otimes\sigma(x,y)\delta\left(t_r-\Delta\tau(t_a)-\frac{R_{mj}(t_a)}{c}\right) \\ &= G\sigma(x,y)s_0(t_r,t_a)\otimes\delta\left(t_r-\Delta\tau(t_a)-\frac{2R_{mj}(t_a)}{c}\right) \end{aligned} \tag{6}$$

where G is the jammer gain factor, $\sigma(x,y)$ is the backscattering coefficient of the false point target. Similarly, the deceptive jamming signal received by the slave antenna is given by

$$J_S(t_r,t_a) = GJ_r(t_r,t_a)\otimes\sigma(x,y)\delta\left(t_r-\Delta\tau(t_a)-\frac{R_{sj}(t_a)}{c}\right) \tag{7}$$

Simultaneously, the real echo signal from the protected target and received by the master antenna can be expressed as

$$s_M(t_r,t_a) = \sigma_{real}(x,y)s_0(t_r,t_a)\otimes\delta\left(t_r-\frac{2R_m(t_a)}{c}\right) \tag{8}$$

where $\sigma_{real}(x,y)$ is the backscattering coefficient of the protected point target. Comparing the time of the unit impulse functions in both (6) and (8), we can derive the time delay $\Delta\tau(t_a)$ as

$$\Delta\tau(t_a) = \frac{2\left(R_m(t_a)-R_{mj}(t_a)\right)}{c} \tag{9}$$

Substituting (5) and (9) into (7), the deceptive jamming signal at the slave antenna can be rewritten as

$$\begin{aligned} &J_S(t_r,t_a) \\ &= G\sigma(x,y)s_0(t_r,t_a)\otimes\delta\left(t_r-\frac{2R_m(t_a)}{c}+\frac{R_{mj}(t_a)}{c}-\frac{R_{sj}(t_a)}{c}\right) \end{aligned} \tag{10}$$

However, the real echo signal from the protected target and received by the slave antenna is given by

$$s_S(t_r,t_a) = \sigma_{real}(x,y)s_0(t_r,t_a)\otimes\delta\left(t_r-\frac{R_m(t_a)+R_s(t_a)}{c}\right) \tag{11}$$

Comparing the time of unit impulse functions in (10) and (11), we can derive the time deviation between the real echo signal and the received deceptive jamming signal at the slave antenna as

$$\Delta\tau_{error}(t_a) = \frac{R_m(t_a)-R_s(t_a)}{c}-\frac{R_{mj}(t_a)-R_{sj}(t_a)}{c} \tag{12}$$

To obtain the distance bias due to the time deviation, we have the following considerations

$$\begin{cases} R_{MJ} = \sqrt{X_s^2+Z_s^2} \\ R_{SJ} = \sqrt{\left(X_s+B\cos(\alpha)\right)^2+\left(Z_s+B\sin(\alpha)\right)^2} \\ R_M = \sqrt{\left(X_s-x\right)^2+\left(Z_s-z\right)^2} \\ R_S = \sqrt{\left(X_s+B\cos(\alpha)-x\right)^2+\left(Z_s+B\sin(\alpha)-z\right)^2} \end{cases} \tag{13}$$

Because the synthetic aperture duration is relatively short for spaceborne InSAR, the inequality $R_{MJ} >> [v_a t_a]$ and $L/2 \geq v_a t_a \geq -L/2$ holds for $R_{MJ} >> [v_a t_a - y]$, $R_{MJ} >> x$, $R_{MJ} >> y$, $R_{MJ} >> z$, and $R_{MJ} >> B$. Accordingly, using the Taylor series expansion, we have the following approximation (As shown in Appendix A)

$$\begin{cases} R_{mj}(t_a) \approx R_{MJ}+\dfrac{(v_a t_a)^2}{2R_{MJ}},\ R_{sj}(t_a) \approx R_{SJ}+\dfrac{(v_a t_a)^2}{2R_{MJ}} \\ R_m(t_a) \approx R_M+\dfrac{(v_a t_a-y)^2}{2R_{MJ}},\ R_s(t_a) \approx R_S+\dfrac{(v_a t_a-y)^2}{2R_{MJ}} \end{cases} \tag{14}$$

According to (12) and (14), we can derive the distance bias $\Delta R_{error}(t_a)$ related to time deviation $\Delta\tau_{error}(t_a)$ as

$$\Delta R_{error}(t_a) = c\Delta\tau_{error}(t_a) \approx (R_M-R_S)-(R_{MJ}-R_{SJ}) \tag{15}$$

From (15), we know that the deceptive interferences at the slave antenna deviate from real echoes from the protected scene, while these at the master antenna completely coincide with the corresponding real signals. The distance bias $\Delta R_{error}(t_a)$ depends heavily on the baseline and the relative position of two antennas, jammer and the protected scene, but not the slow time t_a. Utilizing the system parameters listed in Table I, the relationship between distance bias and distance difference of jammer and protected scene for different baseline values are shown in Fig. 2, where Δx and Δz respectively represent such distance differences along x-axis and z-axis. The increasing distance between jammer and protected scene results in larger distance bias. Particularly when $\Delta x = 0$ and $\Delta z = 0$, the distance bias is negligible. The accuracy of estimation error for the baseline of 200m, as shown in Fig. 3, illustrates the validity of approximation in (15).

After imaging, the distance bias is manifested as the position bias of the false point target along the range dimension. In order to achieve co-registration of the two deceptive scenes, the position bias along the range dimension should be far less than a pixel spacing and it should satisfy $\Delta\tau_{error}(t_a) << 1/(2B_r)$. Therefore, x and z should satisfy

$$(R_M-R_S) << \frac{c}{2B_r}+(R_{MJ}-R_{SJ}) \tag{16}$$

where B_r is the signal bandwidth of the InSAR system.

Impact of Jammer Position on Azimuth Processing

The above analysis indicates that the deceptive scene deviates from the jammed part in the slave image along range, while such deception completely covers the same area in the master image. We now derive the Doppler frequency bias of the false point target in the slave image by using the illustrating geometry, and discuss the influence of azimuth chirp rate estimation error on image focusing.

1) Impact of Jammer Position on Doppler:

In SAR imaging, the 2-D high resolution is achieved by 2-D matched filtering and the large compression gain is obtained by utilizing chirp signals. The relative motion between targets and the satellite leads to the Doppler effect which generates chirp signals along the azimuth direction. In the azimuth dimension, the Doppler frequency satisfies [16]

$$f_a(t_a) = -\frac{2}{\lambda}\frac{dR(t_a)}{dt_a} \tag{17}$$

where λ is the wavelength. Accordingly, the Doppler frequency bias (As shown in Appendix B) of the deceptive jamming signal at the slave antenna can be expressed as

$$\Delta f_a(t_a) = -\frac{1}{\lambda}\frac{d\Delta R_{error}(t_a)}{dt_a} \approx -\frac{v_a{}^2 t_a}{\lambda}(d_1 - d_2) + \frac{v_a y d_1}{\lambda} \quad (18)$$

with $d_1 = \frac{1}{R_M} - \frac{1}{R_S}$ and $d_2 = \frac{1}{R_{MJ}} - \frac{1}{R_{SJ}}$. Fig. 4 shows the Doppler frequency biases for different jamming positions with different baseline values. Clearly, the increasing baseline value results in larger Doppler frequency bias. The Doppler frequency bias will be larger as Δy increases, while it is basically the same as Δx changes. However, such Doppler frequency bias is so small that the position bias of the false point target along the azimuth dimension can be ignored in practice.

2) Impact of Jammer Position on Limit of Azimuth Resolution:

For SAR deceptive jamming, the jammer intercepts chirp signals transmitted by the InSAR system, and then retransmits them after modulation. Since this process does not change the range chirp rate of the deceptive jamming signal at both antennas of InSAR, image along the range dimension is focused. However, in the azimuth dimension, the chirp rate of the deceptive jamming signal is little different from the one of the real echo signal at the slave antenna. The error of the azimuth chirp rate satisfies

$$\Delta K_a = -\frac{1}{\lambda}\frac{d^2\Delta R_{error}(t_a)}{dt_a{}^2}\bigg|_{t_a=t_0} \approx -\frac{v_a{}^2}{\lambda}(d_1 - d_2) \approx 0 \quad (19)$$

where t_0 represents the time corresponding to the nearest distance between the antenna and the real point target and satisfies $t_0 = y / v_a$. Equation (19) indicates that the defocusing of the false point target in the slave image is negligible. Therefore, the jammer position does not affect the azimuth processing of the false point target.

Interferometric Phase of SAR Deceptive Jamming

As the jammer transmits the SAR deceptive jamming signal to InSAR, the deceptive scenes will be generated in two SLC images. Since the interferometry is achieved by measuring the phase difference between dual SAR images, the interferometric phase of the deceptive scenes will further influence phase unwrapping and elevation inversion. If the position bias of the corresponding deceptive scenes is beyond one pixel along the range dimension, the co-registration of these false parts will not be achieved and the deceptive area in the interferogram is shown as phase noise.

We now consider the special circumstance where the position bias of deceptive scenes is ignored and these false parts are accurately co-registered. In order to obtain the interferometric phase of the false point target, the corresponding imaging results are derived through 2-D matched filtering. According to (6), the imaged false point target in the mater image can be obtained as

$$J_{M\_out}(t_r, t_a) = GA\sigma(x,y)\sin c\left(t_r - \frac{2R_M}{c}\right)\sin c(t_a - t_0)\exp\left(-j\frac{4\pi}{\lambda}R_M\right) \quad (20)$$

where A represents the compression gain. Ignoring the position bias along range, the imaging output of the deceptive jamming part in the slave image can be expressed as

$$J_{S\_out}(t_r, t_a) \approx GA\sigma(x,y)\sin c\left(t_r - \frac{R_M + R_S}{c}\right)\sin c(t_a - t_0) \cdot \exp\left(-j\frac{4\pi}{\lambda}R_M\right)\exp\left(j\frac{2\pi}{\lambda}(R_{MJ0} - R_{SJ0})\right) \quad (21)$$

with

$$R_{MJ0} = \sqrt{X_s{}^2 + y^2 + Z_s{}^2} \quad (21a)$$

$$R_{SJ0} = \sqrt{(X_s + B\cos(\alpha))^2 + y^2 + (Z_s + B\sin(\alpha))^2} \quad (21b)$$

After co-registration, we derive the phase difference of (20) and (21) through conjugate multiplication as

$$\Delta\phi = -\frac{2\pi}{\lambda}(R_{MJ0} - R_{SJ0}) \approx -\frac{2\pi}{\lambda}(R_{MJ} - R_{SJ}) \quad (22)$$

Equation (22) indicates that the interferometric phase of the false point target is approximated as a constant, which depends on the nearest distances between the dual antennas and the jammer. Moreover, even if the deceptive jamming signal is transmitted with expected phase, it is impossible to achieve InSAR deceptive interference based on 3-D model for the expected phase will be eliminated completely through conjugate multiplication. Therefore, SAR deceptive jamming can only play a very limited role for InSAR systems.

3-D Deceptive Jamming Algorithm

In section II, it has been shown that the SAR deceptive scene, due to the limitation of a single jammer, can be discovered by interferometry. To overcome the problem and achieve effective achieve 3-D deceptive jamming, a joint interfering method based on multiple jammers is proposed in this part. According to Fig. 1, now the jamming effects are produced by both jammers J_1 and J_2. For this jamming method, we first make sure that the specific geographic location of the two jammers meets the limiting conditions discussed in the former section. Next, the expected terms for the two jammers are generated according to the deceptive phase and the relative positions between dual antennas and the two jammers. Finally, the jamming signals are decomposed into the slow-time-independent terms which are generated off-line and the slow-time-dependent terms which are derived from 1-D real-time frequency modulation. Such jamming signals with the specific terms are convolved with the intercepted SAR signals. Detailed steps are introduced as follows.

Constant Terms for the Two Jammers

We now combine the two jammers J_1 and J_2 to produce 3-D deceptive scene. Suppose that the deceptive jamming signals of the two jammers are multiplied with different

complex constants. According to (20), the 2-D matched filter output for the deceptive jamming signal transmitted by J_1 and received by the master antenna can be expressed as

$$J_{M\_out}(t_r,t_a)=GA\sigma(x,y)\cdot\sin c\left(t_r-\frac{2R_M}{c}\right)\sin c(t_a-t_0)\exp\left(-j\frac{4\pi}{\lambda}R_M\right)\cdot U(x,y) \quad (23)$$

where $U(x,y)$ is the complex constant generated by J_1. As the jammer J_1 is placed under the condition of (16), the position bias of the false target in the slave image can be ignored. Then, according to (21), the false point target in the slave image is given by

$$J_{S\_out}(t_r,t_a)\approx GA\sigma(x,y)\sin c\left(t_r-\frac{R_M+R_S}{c}\right)\sin c(t_a-t_0)\cdot\exp\left(-j\frac{4\pi}{\lambda}R_M\right)\exp\left(j\frac{2\pi}{\lambda}(R_{MJ0}-R_{SJ0})\right)\cdot U(x,y) \quad (24)$$

Similarly, for the same protected target, the imaged deceptive jamming from J_2 for dual antennas are respectively expressed as

$$J'_{M\_out}(t_r,t_a)=GA\sigma(x,y)\cdot\sin c\left(t_r-\frac{2R_M}{c}\right)\sin c(t_a-t_0)\exp\left(-j\frac{4\pi}{\lambda}R_M\right)\cdot V(x,y) \quad (25)$$

$$J'_{S\_out}(t_r,t_a)=GA\sigma(x,y)\sin c\left(t_r-\frac{R_M+R_S}{c}\right)\sin c(t_a-t_0)\cdot\exp\left(-j\frac{4\pi}{\lambda}R_M\right)\exp\left(j\frac{2\pi}{\lambda}(R'_{MJ0}-R'_{SJ0})\right)\cdot V(x,y) \quad (26)$$

Therefore, we have

$$J_{M\_sum}(t_r,t_a)=J_{M\_out}(t_r,t_a)+J'_{M\_out}(t_r,t_a)=GA\sigma(x,y)\sin c\left(t_r-\frac{2R_M}{c}\right)\sin c(t_a-t_0)\exp\left(-j\frac{4\pi}{\lambda}R_M\right)\cdot\left(U(x,y)+V(x,y)\right) \quad (27)$$

$$J_{S\_sum}(t_r,t_a)=J_{S\_out}(t_r,t_a)+J'_{S\_out}(t_r,t_a)=GA\sigma(x,y)\sin c\left(t_r-\frac{2R_M}{c}\right)\sin c(t_a-t_0)\exp\left(-j\frac{4\pi}{\lambda}R_M\right)\cdot\left\{\begin{array}{l}\exp\left(j\frac{2\pi}{\lambda}(R_{MJ0}-R_{SJ0})\right)U(x,y)\\+\exp\left(j\frac{2\pi}{\lambda}(R'_{MJ0}-R'_{SJ0})\right)V(x,y)\end{array}\right. \quad (28)$$

After co-registration and conjugate multiplication of two SLC images, the phase difference between $J_{M\_sum}(t_r,t_a)$ and $J_{S\_sum}(t_r,t_a)$ is given by

$$arg\left[J_{M\_sum}(t_r,t_a)\cdot J_{S\_sum}{}^{*}(t_r,t_a)\right]=\Delta\varphi_{false}(x,y) \quad (29)$$

where $\arg[\cdot]$ is the operation of taking the phase information, $\Delta\varphi_{false}(x,y)$ is supposed to be the desired phase. Combining (27), (28) and (29), we obtain the constant terms for J_1 and J_2 as

$$U(x,y)=\frac{\exp\left(j\frac{2\pi}{\lambda}(R'_{MJ0}-R'_{SJ0})\right)-\exp\left(-j\Delta\varphi_{false}(x,y)\right)}{\Delta\varphi_0} \quad (30)$$

$$V(x,y)=\frac{\exp\left(-j\Delta\varphi_{false}(x,y)\right)-\exp\left(j\frac{2\pi}{\lambda}(R_{MJ0}-R_{SJ0})\right)}{\Delta\varphi_0} \quad (31)$$

with

$$\Delta\varphi_0=\exp\left(j\frac{2\pi}{\lambda}(R'_{MJ0}-R'_{SJ0})\right)-\exp\left(j\frac{2\pi}{\lambda}(R_{MJ0}-R_{SJ0})\right) \quad (32)$$

where $\Delta\varphi_0$ is a nonzero constant. Especially when $\Delta\varphi_0=0$, the deceptive phase in the interferogram will disappear. Thus, this particular case should be avoided. Equations (30) and (31) indicate that when the deceptive jamming signals with terms $U(x,y)$ and $V(x,y)$ are simultaneously transmitted from the two jammers, the deceptive phase $\Delta\varphi_{false}(x,y)$ will be derived through interferometry, which will ultimately produce the expected false DEM.

Fast 3-D Deceptive Jamming

Based on the constant terms obtained in the former section, the transmitting signals from the two jammers will be derived. To transmit the jamming signals very quickly, a fast scene deceptive jamming algorithm is provided in this section [16]. According to (6), the transmitting signal of J_1 can be expressed as

$$J_1(t_r,t_a)=GJ_{r1}(t_r,t_a)\otimes\sigma(x,y)\delta\left(t_r-\frac{2\left(R_m(t_a)-R_{mj}(t_a)\right)}{c}\right)\cdot U(x,y) \quad (33)$$

where $J_{r1}(t_r,t_a)$ denotes the real echo signal received by J_1. Performing FFT to (33) along the fast time t_r yields

$$J_1(f_r,t_a)=G\sigma(x,y)J_{r1}(f_r,t_a)\exp\left(-j\frac{4\pi f_r}{c}\left(R_m(t_a)-R_{mj}(t_a)\right)\right)\cdot U(x,y) \quad (34)$$

where $J_{r1}(f_r,t_a)$ is the Fourier transform of $J_{r1}(t_r,t_a)$ along t_r. Using the Taylor series expansion at slow time t_a (As shown in Appendix C), we have the following approximation

$$R_m(t_a)-R_{mj}(t_a)=\left(R_{M0}-R_{MJ}\right)-\frac{yv_at_a}{R_{M0}}+\frac{\left(v_at_a\right)^2}{2}\left(\frac{1}{R_{M0}}-\frac{1}{R_{MJ}}\right) \quad (35)$$

with

$$R_{M0}=\sqrt{\left(X_s-x\right)^2+y^2+\left(Z_s-z\right)^2} \quad (35a)$$

Substituting (35) into (34), the transmitting signal from J_1 can be rewritten as

$$J_1(f_r,t_a)=GJ_{r1}(f_r,t_a)\underbrace{\sum_{x,y}\sigma(x,y)F_1(x,y)F_2(x,y)}_{Part\ I} \quad (36)$$

with

$$F_1(x,y)=\exp\left(-j2\pi f_r\left(R_{M0}-R_{MJ}\right)\right)\cdot U(x,y) \tag{36a}$$

$$F_2(x,y)=\exp\left\{j2\pi f_r\left[\frac{yv_at_a}{R_{M0}}-\frac{\left(v_at_a\right)^2}{2}\left(\frac{1}{R_{M0}}-\frac{1}{R_{MJ}}\right)\right]\right\} \tag{36b}$$

In (36), R_{MJ} can be obtained according to the satellite orbit parameters, and R_{M0} can be derived from the relationship between the protected targets. Therefore, R_{MJ} and R_{M0} are predefined before the jamming is carried out. It is technically feasible to calculate $F_1(x,y)$ in advance. However, $F_2(x,y)$ depends heavily on t_a, and it is generated in real time. Similarly, we obtain the transmitting signal from J_2 as

$$J_2(f_r,t_a)=GJ_{r2}(f_r,t_a)\underbrace{\sum_{x,y}\sigma(x,y)F_3(x,y)F_4(x,y)}_{Part\ II} \tag{37}$$

with

$$F_3(x,y)=\exp\left(-j2\pi f_r\left(R'_{M0}-R'_{MJ}\right)\right)\cdot V(x,y) \tag{37a}$$

$$F_4(x,y)=\exp\left\{j2\pi f_r\left[\frac{yv_at_a}{R'_{M0}}-\frac{\left(v_at_a\right)^2}{2}\left(\frac{1}{R'_{M0}}-\frac{1}{R'_{MJ}}\right)\right]\right\} \tag{37b}$$

In this way, 3-D deceptive jamming will be realized as the two jammers J_1 and J_2 simultaneously transmit the deceptive jamming signals obtained by convolving the intercepted echo signals with different terms as show in *Part I* and *Part II* in (36) and (37).

Analysis of Jamming Coverage in 2-D

In Range: the analysis in section II indicates that the coverage of deceptive jamming along range is determined by the position bias of the false point targets, which is shown in (16). Meanwhile, to avoid azimuth defocusing, the coverage of deceptive scene along range should satisfy

$$\sqrt{x^2+z^2}<\frac{\lambda R_{MJ}^{\ 2}}{2\left(T_av_a\right)^2} \tag{38}$$

where T_a is the coherent integration time. Therefore, the predesigned position of the deceptive scene should satisfy (16) and (38) simultaneously.

In Azimuth: from the former section, the Doppler frequency error and azimuth chirp rate error of the false echoes are negligible. The coverage of deceptive jamming is determined by the pulse repetition frequency (PRF). The instantaneous slant-range history of an idea point target is different from the one of the corresponding false point target, which will lead to Doppler ambiguity and produce the ghost image along azimuth [16]. Considering the windowing processing in practice, the coverage of the deceptive jamming along azimuth should satisfy

$$\left|y\right|\le\frac{\lambda\cdot R_{MJ}\left(PRF-v_a/D\right)}{2v_a}-\frac{L}{2} \tag{39}$$

where D denotes the antenna aperture in azimuth, L represents the synthetic aperture length.

Simulations and Analysis

The aforementioned sections have analyzed the SAR deceptive effects for single-pass spaceborne InSAR and addressed procedures of 3-D deceptive jamming by combining two jammers, together with detailed theoretical analysis. In what follows, to demonstrate interfering effects of SAR deceptive jamming and our proposed method, simulation results are provided based on the TanDEM-X system [25].

Analysis of Position Bias

In this part, we will analyze the position bias caused by the relative distance between the jammer and the protected scene. The point targets are generated using the Chirp-Scaling algorithm with the system parameters listed in Table I [26]. Suppose that the jammer is located at (0, 0) km. The real point targets are equally distributed from -4 to 4 km with a 1 km interval along range and share the same azimuth coordinate 0 km.

To derive the position bias in the slave image, it is supposed that these real point targets in the master image are completely covered by the corresponding false targets. In the slave image, as shown by Fig. 5, seven false point targets are superimposed upon the same number of real ones. Fig. 5(a) illustrates the jammed image with the baseline of 200m, while these baselines of 500m and 800m are shown in Fig. 5(b) and Fig. 5(c). From Fig. 5(a), it is observed that the real point target and the corresponding false one almost coincide, and the phase of the complex data is partly cancelled. Therefore, the target slight target offset is inevitable after imaging. In each sub-figure of Fig. 5, the range position bias between the real point target and the corresponding one becomes larger as the distance between jammer and protected target increases, while the azimuth position bias can be ignored. Particularly when the false point target is located at the jammer position, the position bias is 0. Among these three figures, the increasing baseline value results in larger range position bias. Therefore, to precisely cover real signals from the protected scene in two SAR images, the distance between jammer and deceptive scene should be appropriately reduced.

SAR Deceptive Effects on Imaging and Interferometry

To show the ineffectiveness of the SAR deceptive jamming, a terrain with an area of 4096 m×4096 m (ground range and azimuth direction) is considered. The system parameters are listed in Table I and those for the simulation scenarios are listed in Tables II. To avoid the position bias of the deceptive scene, a single jammer is placed at the center of the deceptive scene. The processing procedures of InSAR involve SAR imaging, relevant registration, and interferometry. Finally, the effects of the SAR deceptive jamming on interferometric phase are well understood through simulation.

Since the original echo signals and the deceptive jamming signal are received by the two antennas simultaneously, simulation of SAR echo signals with such jamming is first

performed. Without loss of generality, only the original master image is shown in Fig. 6(a). We choose Fig. 6(b) as the deceptive jamming template according to the prior knowledge of targets around the coastal area. Assuming that the jamming to signal ratio (JSR) is 0dB, the master image with the traditional SAR deceptive jamming transmitted by the single jammer is presented in Fig. 6(c). Through co-registration and comparing both complex images, the resultant interferometric phase is obtained and depicted in Fig. 7(b). For comparison purposes, the original interferometric phase without jamming is shown in Fig. 7(a). By comparing Fig. 7(a) and (b), the deceptive part in the interferogram is clearly visible. As can be seen, the phase of the deceptive scene achieves effective cancellation and will introduce noisy changes to the unwrapped phase.

Since the interferometric phase is wrapped into the interval $[-\pi,\pi]$, it must be unwrapped before being converted it to elevation result. After phase filtering, the unwrapped phase including the jamming effect is derived through the branch-cut phase unwrapping method [27], [28]. Finally, DEM is produced according to the geometric relationship of the scene. Fig. 8 presents the generated DEM before and after SAR deceptive jamming, where the false part in Fig. 8(b) can be seen clearly and the elevation of surrounding area is also affected. Even if the false phase is added for the false echo, such cancellation is inevitable. Therefore, the SAR deceptive jamming will not work for the single-pass spaceborne InSAR.

3-D Deceptive Jamming Based on Three-Step Processing

The aforementioned problems are effectively solved by the proposed algorithm in three steps: 1) determine the jammer locations; 2) predesign the false elevation and obtain the expected terms; and 3) convolve the intercepted SAR signals with the expected terms. The simulated data will be generated as follows.

In practice, we predict the trajectory of a satellite travelling along the sun-synchronous orbit by utilizing the satellite tool kit software [16]. The positions of two jammers (As shown in Table III) are determined by the restriction of position bias and $\Delta\varphi_0$ of (32). The interference range should meet the coverage requirements of (38) and (39).

Fig. 6(a) presents the original master image without jamming. As the two jammers retransmit the convolved signals simultaneously, the imaging result at the master antenna is shown in Fig. 9(a). Although Fig. 9(a) and Fig. 6(c) look the same, they are achieved by different jamming method. Therefore, the interferometric results are different from each other. Fig. 9(b) is the generated interferogram with deceptive phase. Compared with Fig. 7(b), the deceptive phase instead of phase noise is superimposed upon the original phase part. Fig. 9(c) shows the DEM with 3D deception. By comparing Fig. 8(a) and Fig. 9(c), false elevation has been generated as expected, again demonstrating the good performance of the proposed jamming algorithm.

CONCLUSIONS

In this paper, the interfering effect of SAR deceptive jamming has been analyzed and a novel 3-D deceptive jamming method jointly employing two jammers has been proposed. The 3-D deceptive jamming method can produce false elevation in the final DEM of a single-pass spaceborne InSAR system. Moreover, the following four major findings have been obtained:

(1) Whether it is for a single jammer or two jammers, the relative position between the jammer and the protected target will cause the position bias of the false point target along range in the resultant SAR images, which will further affect the co-registration of the deceptive scenes.

(2) For traditional SAR deceptive jamming using by a single jammer, the predesigned deceptive phase is inevitably cancelled by interferometry, even if co-registration is completely achieved.

(3) With the proposed jamming algorithm, the imaging results with deceptive scenes will produce the interferogram with deceptive phase.

(4) The generated phase after inversion is manifested as DEM with false elevation information.

As also shown by our simulation results based on the TanDEM-X system, the proposed algorithm can effectively deceive the InSAR system and shows great promise in the field of electronic warfare. Furthermore, this jamming method also reveals a weak point of current InSAR systems, which provides a starting point for improving the performance and robustness of InSAR systems. Study on the limits of constant terms for the two jammers and 3-D deceptive jamming for dual-pass spaceborne InSAR will be topics of our future reseach.

APPENDIX A

This part will analyze the influence of approximation on accuracy of the distance bias $\Delta R_{error}(t_a)$. In (14), the partial second-order and the higher-order terms of Taylor series expansion are neglected. If the full second-orders terms are preserved, (14) changes to

$$\begin{cases} R_{mj}(t_a)=\sqrt{R_{MJ}{}^2+(v_a t_a)^2}\approx R_{MJ}+\dfrac{(v_a t_a)^2}{2R_{MJ}} \\ R_{sj}(t_a)=\sqrt{R_{SJ}{}^2+(v_a t_a)^2}\approx R_{SJ}+\dfrac{(v_a t_a)^2}{R_{SJ}} \\ R_m(t_a)=\sqrt{R_M{}^2+(v_a t_a-y)^2}\approx R_M+\dfrac{(v_a t_a-y)^2}{2R_M} \\ R_s(t_a)=\sqrt{R_S{}^2+(v_a t_a-y)^2}\approx R_S+\dfrac{(v_a t_a-y)^2}{2R_S} \end{cases} \tag{A1}$$

According to (12) and (A1), the position bias $\Delta R_{error}(t_a)$ is derived as

$$\Delta R_{error}(t_a) \approx (R_M - R_S) - (R_{MJ} - R_{SJ}) + \frac{1}{2}\left(\frac{1}{R_M} - \frac{1}{R_S}\right)(v_a t_a - y)^2 - \frac{1}{2}\left(\frac{1}{R_{MJ}} - \frac{1}{R_{SJ}}\right)(v_a t_a)^2$$
$$\approx (R_M - R_S) - (R_{MJ} - R_{SJ}) - \frac{1}{2}\left(\frac{B\sin(\theta\text{-}\alpha)}{R_M R_S}\right)(v_a t_a - y)^2 + \frac{1}{2}\left(\frac{B\sin(\theta_J\text{-}\alpha)}{R_{MJ} R_{SJ}}\right)(v_a t_a)^2 \quad \text{(A2)}$$

where θ and θ_J respectively denote the look angles of the master antenna corresponding to the protected point target and the jammer. Since $R_M R_S >> B\sin(\theta\text{-}\alpha)$ and $R_{MJ} R_{SJ} >> B\sin(\theta_J\text{-}\alpha)$, the last two terms of (A2) can be neglected. Then, (A2) changes to

$$\Delta R_{error}(t_a) \approx (R_M - R_S) - (R_{MJ} - R_{SJ}) \quad \text{(A3)}$$

Fig. 10 shows the estimation error caused by the approximation for different baseline values within one synthetic aperture time, while Fig. 11 presents the corresponding percentage of such an estimation error. As can be seen, the estimation error of the position bias is less than 0.015m, and the percentage of this estimation error is much less than 0.5%. Therefore, the approximation of (A3) is reasonable.

APPENDIX B

This appendix will give details of the calculation of $\Delta f_a(t_a)$. According to (11) and (17), we can obtain the Doppler frequency of the real echo signal in the slave image as

$$f_{a\_real}(t_a) = -\frac{1}{\lambda}\frac{d\left(R_m(t_a) + R_s(t_a)\right)}{dt_a} \quad \text{(B1)}$$

Similarly, the Doppler frequency of received deceptive jamming signal corresponding to the real echo signal is expressed as

$$f_{a\_false}(t_a) = -\frac{1}{\lambda}\frac{d\left(2R_m(t_a) - R_{mj}(t_a) + R_{sj}(t_a)\right)}{dt_a} \quad \text{(B2)}$$

Comparing (B1) and (B2), we have

$$\Delta f_a(t_a) = -\frac{1}{\lambda}\frac{d\left(R_m(t_a) - R_s(t_a) - R_{mj}(t_a) + R_{sj}(t_a)\right)}{dt_a}$$
$$= -\frac{1}{\lambda}\left(v_a(v_a t_a - y)\left(\frac{1}{R_m(t_a)} - \frac{1}{R_s(t_a)}\right) - v_a^2 t_a\left(\frac{1}{R_{mj}(t_a)} - \frac{1}{R_{sj}(t_a)}\right)\right) \quad \text{(B3)}$$

Substituting (14) into (B3), the Doppler frequency bias can be rewritten as

$$\Delta f_a(t_a) \approx -\frac{v_a^2 t_a}{\lambda}\left(\frac{1}{R_M} - \frac{1}{R_S} - \frac{1}{R_{MJ}} + \frac{1}{R_{SJ}}\right) + \frac{v_a y}{\lambda}\left(\frac{1}{R_M} - \frac{1}{R_S}\right) \quad \text{(B4)}$$

APPENDIX C

Using the Taylor series expansion at t_a, $R_m(t_a)$ becomes

$$R_m(t_a) \approx \sqrt{(X_s - x)^2 + y^2 + (Z_s - z)^2} - \frac{y v_a t_a}{\sqrt{(X_s - x)^2 + y^2 + (Z_s - z)^2}} + \frac{(v_a t_a)^2}{2\sqrt{(X_s - x)^2 + y^2 + (Z_s - z)^2}} = R_{M0} - \frac{y v_a t_a}{R_{M0}} + \frac{(v_a t_a)^2}{2R_{M0}} \quad \text{(C1)}$$

Similarly, $R_{mj}(t_a)$ can be rewritten

$$R_{mj}(t_a) \approx \sqrt{X_s^2 + Z_s^2} + \frac{v_a t_a^2}{2\sqrt{X_s^2 + Z_s^2}} = R_{MJ} + \frac{v_a t_a^2}{2R_{MJ}} \quad \text{(C2)}$$

Therefore, we obtain the difference between $R_m(t_a)$ and $R_{mj}(t_a)$ as

$$R_m(t_a) - R_{mj}(t_a) = (R_{M0} - R_{MJ}) - \frac{y v_a t_a}{R_{M0}} + \frac{(v_a t_a)^2}{2}\left(\frac{1}{R_{M0}} - \frac{1}{R_{MJ}}\right) \quad \text{(C3)}$$

REFERENCES

[1] L. Xiaoming, S. Lehner, and W. Rosenthal, "Investigation of ocean surface wave refraction using TerraSAR-X data," IEEE Transactions on Geoscience and Remote Sensing, vol. 48, no. 2, pp. 830-840, Feb. 2010.

[2] R. Romeiser, H. Runge, "Theoretical evaluation of several possible along-track InSAR modes of TerraSAR-X for ocean current measurements," IEEE Transactions on Geoscience and Remote Sensing, vol. 45, no. 1, pp. 21-35, Jan. 2007.

[3] R. Romeiser, S. Suchandt, H. Runge, et al. "First analysis of TerraSAR-X along-track InSAR-derived current fields," IEEE Transactions on Geoscience and Remote Sensing, vol. 48, no. 2, pp. 820-829, Feb. 2010.

[4] Q. Liu, S. Xing, X. Wang, et al. "The Interferometry phase of InSAR coherent jamming with arbitrary waveform modulation," Progress In Electromagnetics Research, 2012.

[5] T. Bo and W. Weiyan, "The Study of the Characteristic of InSAR in ECCM," Journal of Electronics and Information Technology, vol. 28, no. 10, pp. 1809-1811, 2006.

[6] T. Bo, "Effect of Jammer Motion on Two Channels Cancellation in InSAR EW," Infrared and Laser Engineering, vol. 37, Supplement, pp. 719-722, Jun. 2008.

[7] R. Schroer, "Electronic warfare," IEEE Aerospace and Electronic Systems Magazine, vol. 18, no. 7, pp. 49-54, Jul. 2003.

[8] N. Li and Y. Zhang, "A survey of radar ECM and ECCM," IEEE Transactions on Aerospace and Electronic Systems, vol. 31, no. 3, pp. 1110-1120, Jul. 1995.

[9] L. Jia, X. Jia, et al. "Analysis on the Effects of Rebound Jamming on InSAR Imaging," Electronic Information Warfare Technology, vol. 27, no. 3, 2012.

[10] B. Ding, M. S. Xiang, and X. D. Liang, "Analysis of the effect of radio frequency interference on interferometric phase," Geoscience and Remote Sensing Symposium, pp. 4628-4631, Jul. 2010.

[11] Y. Ma J. Cai and H. Zang, "An Technique Evaluating of the Barrage Jamming Effect on SAR," Modern Radar, vol. 10, no. 001, 2004.

[12] D. S. Garmatyuk and R. M. Narayanan, "Ultra-wideband continuous-wave random noise arc-SAR," IEEE Transactions on Geoscience and Remote Sensing, vol. 40, no. 12, pp. 2543-2552, Dec 2002.

[13] M. Soumekh, "SAR-ECCM using phase-perturbed LFM chirp signals and DRFM repeat jammer penalization," IEEE Transactions on Aerospace and Electronic Systems, vol.42, no. 2, pp. 191-205, Jan. 2006.

[14] K. Dumper, "Spaceborne synthetic aperture radar and noise jamming," In Proceedings of the IEE International Radar Conference, Edinburgh, U.K., pp. 411-417, 1997.

[15] L. Tao, C. Weidong, L. Guanghua, and W. Dongjin, "A study on scatter-wave jamming for countering SAR," International Conference on Microwave and Millimeter Wave Technology, pp. 1-4, Apr. 2007.
[16] Z. Feng, Z. Bo, T. Mingliang, B. Xueru, C. Bo, S. Guangcai, "A Large Scene Deceptive Jamming Method for Space-Borne SAR," IEEE Transactions on Geoscience and Remote Sensing, vol. 51, no.8, pp. 4486-4495, Aug. 2013.
[17] S. Long, Z. Hongrong, T.Yuesheng, et al. "Research on deceptive jamming technologies against SAR," 2009. APSAR 2009. 2nd Asian-Pacific Conference on Synthetic Aperture Radar, pp. 521-525, Oct. 2009.
[18] X. Lin, P. Liu, G. Xue, "Fast generation Of SAR deceptive jamming signal based on inverse Range Doppler algorithm," IET International Radar Conference 2013, pp. 1-4, 2013.
[19] W. Wang, J. Cai, "A technique for jamming bi-and multistatic SAR systems," IEEE Geoscience and Remote Sensing Letters, vol. 4, no. 1, pp. 80-82, Jan. 2007.
[20] S. L. Wang, L. Yu, J. L. Ni, and G. Y. Zhang, "A study on the active deception jamming to SAR," Acta Electronica Sinica, vol. 31, no. 12, pp. 1900-1902. 2003.
[21] P. E. Pace, D. J. Fouts, S. Ekestorm, and C. Karow, "Digital false target image synthesiser for countering ISAR," IEE Proc. Radar Sonar Navigat., vol. 149, no. 5, pp. 248-257, Oct. 2002.
[22] J. Li, J. Xin, Y. Canbin, et al., "Research on jamming to interferometric synthetic aperture radar," Aerospace Electronic Warfare, vol. 26, no. 4, pp. 30-33, 2010.
[23] Q. Wang, "Synthetic Aperture Radar Technique Against Interferometric Research on Deception Jamming [D]," Xidian University, 2013.
[24] B. Tang, K. Guo, J. Wang, "The 3D Active Deception Jamming of SAR," Acta Electronica Sinica, vol. 35, no. 6, pp. 1203-1206, Jun. 2007.
[25] G. Krieger, A. Moreira, H. Fiedler, et al., "TanDEM-X: A Satellite Formation for High-Resolution SAR Interferometry," IEEE Transactions on Geoscience and Remote Sensing, vol. 45, no. 11, pp. 3317-3341, Nov. 2007.
[26] R. K. Raney, H. Runge, R. Bamler, et al., "Precision SAR processing using chirp scaling," IEEE Transactions on Geoscience and Remote Sensing, vol.32, no. 4, pp. 786-799, Jul. 1994.
[27] L .Mingsheng, W. Teng, L. Lijun, Z. Wenjun, and L. Deren, "Reconstruction of DEMs from ERS-1/2 Tandem Data in mountainous area facilitated by SRTM," IEEE Transactions on Geoscience and Remote Sensing, vol. 45, no. 7, pp. 2325-2335, Jul. 2007.
[28] L. Zhenfang, B.Zheng, and S.Zhiyong, "A joint image coregistration Phase Noise Suppression, and Phase Unwrapping Method Based on Subspace Projection for Multibaseline InSAR Systems," IEEE Transactions on Geoscience and Remote Sensing, vol. 45, no. 3, pp. 584-591, Mar. 2007.

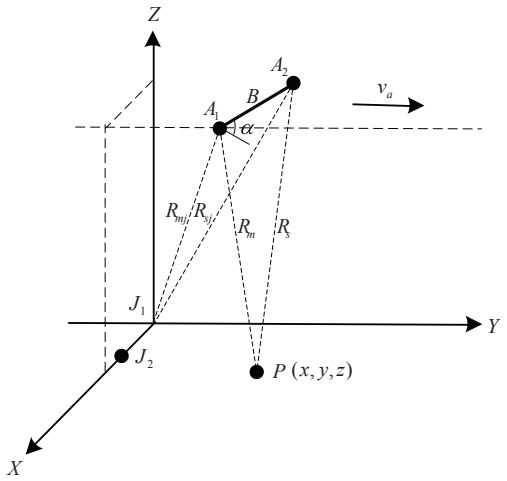

Fig. 1. InSAR and Jammers geometry

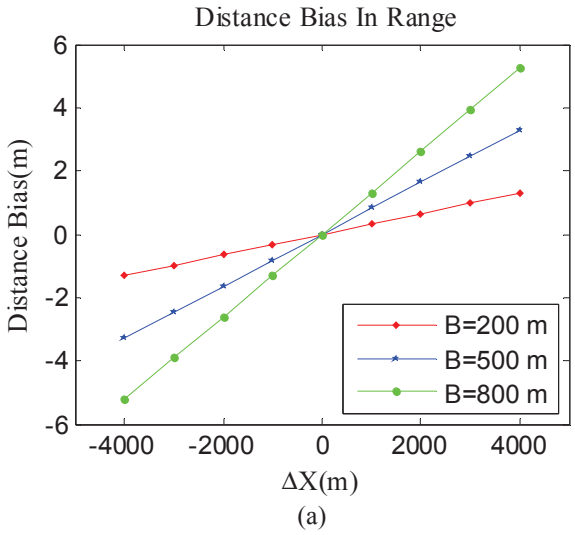

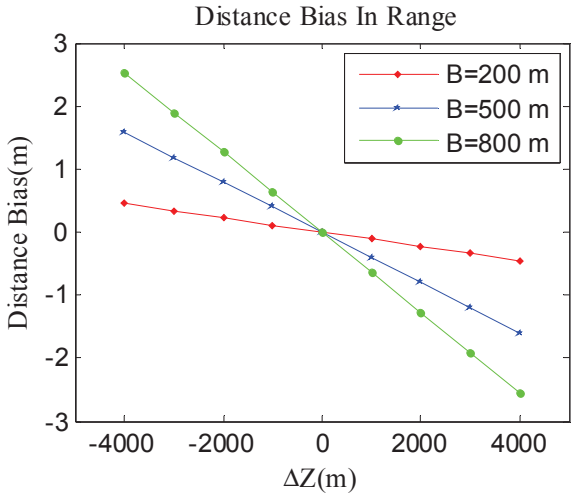

Fig. 2. The impact of Δx (a) and Δz (b) on distance bias with different baselines.

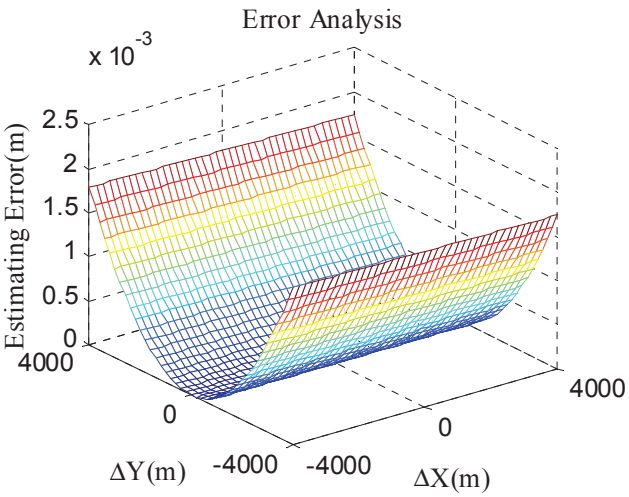

Fig. 3. The influence of approximation on computational accuracy as the baseline is 200m.

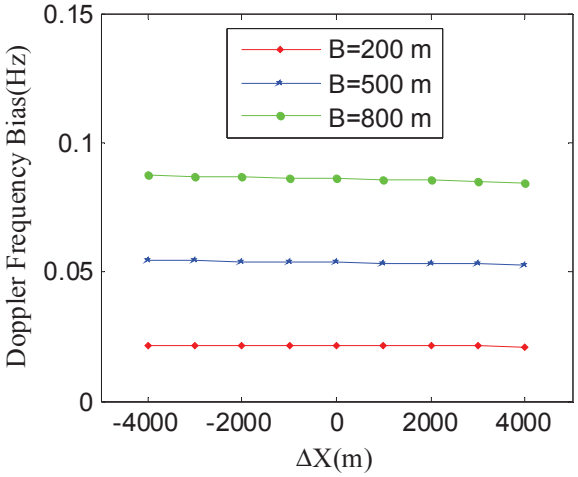

(a)

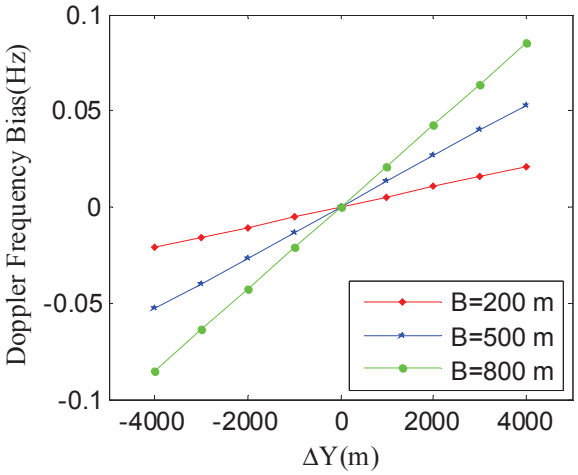

(b)

Fig. 4. The impact of Δx (a) and Δy (b) on Doppler frequency bias with different baselines.

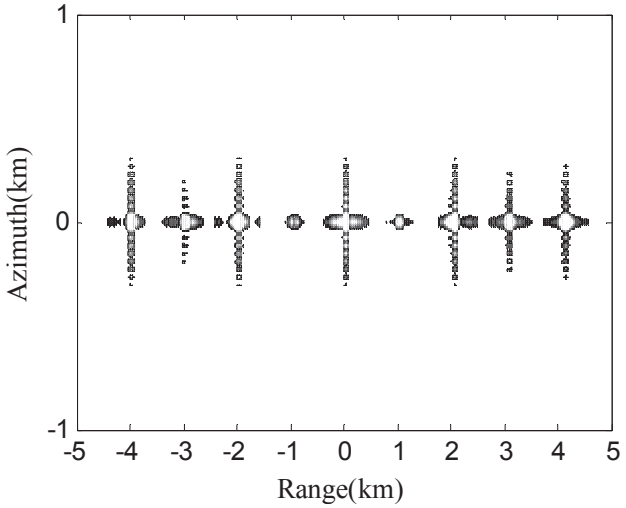

(a)

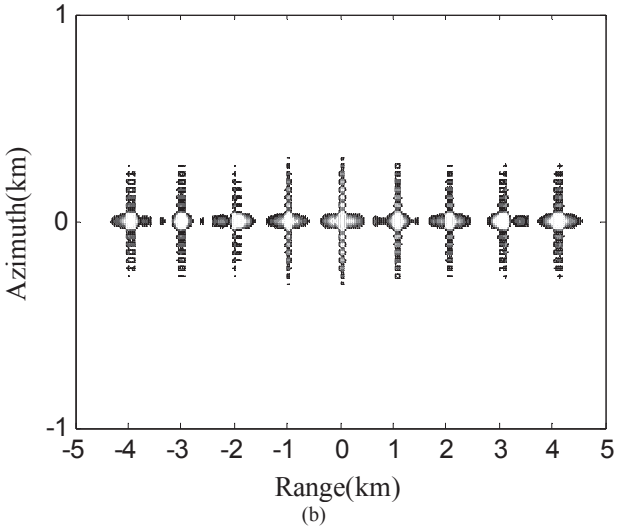

(b)

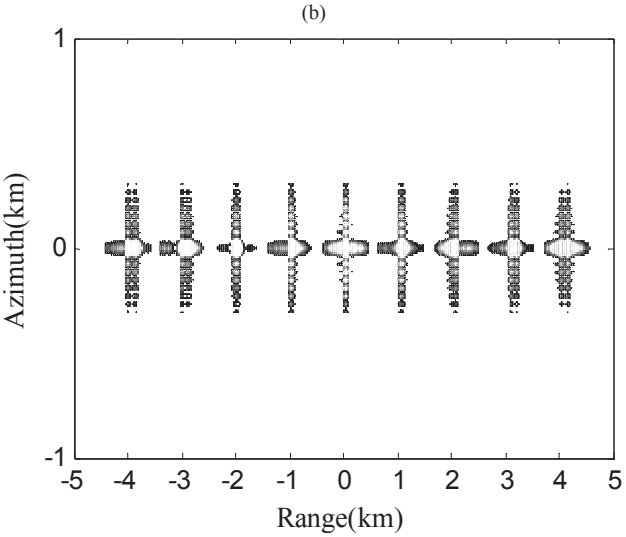

(c)

Fig. 5. Distance bias in the salve image with different baselines. (a) 200m. (b) 500m. (c) 800m.

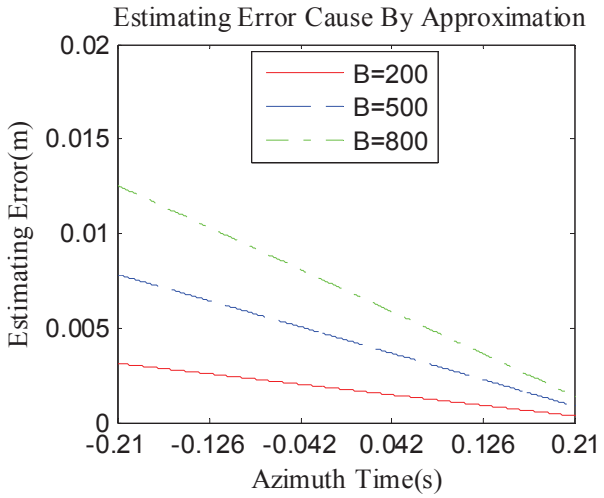

Fig. 10. The impact of approximation on estimation error for different baselines with $\Delta x = 4000$ and $\Delta z = 4000$.

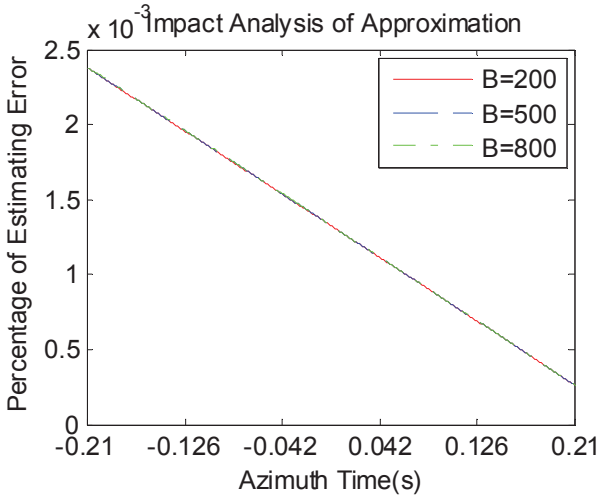

Fig. 11. The percentage of estimation error corresponding to Fig. 10.

TABLE I
SIMULATION PARAMETERS OF THE INSAR SYSTEM

Parameter	Value
Carrier frequency	9.6GHz
Chirp rate	1.3×10^{13} Hz/s
Pulse duration	10μs
Sampling frequency	145MHz
Sensor velocity	7604m/s
Squint angle	0°
Altitude	514.8km
Baseline length	200m
Baseline inclination	0°

TABLE II
SIMULATION PARAMETERS OF THE SCENE

Parameter	Value
Range point number	4096
Azimuth point number	4096
Interval along range	1m
Interval along azimuth	1m

TABLE III
PARAMETERS OF TWO JAMMERS

Jammer Number	Location
Jammer 1	(0,0,0)km
Jammer 2	(0,200,0)km